The Astrophysical Journal, 941:69 (12pp), 2022 December 10 https://doi.org/10.3847/1538-4357/aca016

Discovery of a Double Sequence of Blue Straggler Stars in the Core-collapsed Globular Cluster NGC 6256

Mario Cadelano[1,2], Francesco R. Ferraro[1,2], Emanuele Dalessandro[2], Barbara Lanzoni[1,2], Cristina Pallanca[1,2], and Sara Saracino[2,3]
[1] Dipartimento di Fisica e Astronomia, Universit di Bologna, Via Gobetti 93/2 I-40129 Bologna, Italy; mario.cadelano@unibo.it
[2] INAF-Osservatorio di Astrofisica e Scienze dello Spazio di Bologna, Via Gobetti 93/3 I-40129 Bologna, Italy
[3] Astrophysics Research Institute, Liverpool John Moores University, 146 Brownlow Hill, Liverpool, L3 5RF, UK
Received 2022 June 21; revised 2022 October 14; accepted 2022 November 2; published 2022 December 13

Abstract

We used a combination of high-resolution optical images acquired with the Hubble Space Telescope and near-IR wide-field data to investigate the stellar density profile and the population of blue straggler stars (BSSs) in the Galactic globular cluster NGC 6256, with the aim of probing its current stage of internal dynamical evolution. We found that the inner stellar density profile significantly deviates from a King model, while it is well reproduced by a steep cusp with a power-law slope $\alpha_{\rm cusp} = -0.89$, thus implying that the cluster is currently in the post-core-collapse (PCC) phase. This is also confirmed by the very high segregation level of the BSS population measured through the $A^+_{\rm rh}$ parameter. We also found that the distribution of BSSs in the color–magnitude diagram is characterized by a collimated blue sequence and a red more sparse component, as already observed in three other PCC clusters. A comparison with appropriate collisional models demonstrates that the vast majority of the BSSs lying along the collimated blue sequence is consistent with a generation of coeval (1 Gyr old) stars with different masses originated by an event that highly enhanced the collisional rate of the system (i.e., the core collapse). This study confirms that the segregation level of BSSs is a powerful dynamical diagnostic also of star cluster in a very advanced stage of dynamical evolution. Moreover, it pushes forward the possibility of using the morphology of BSSs in a color–magnitude diagram as a tracer of the core-collapse and subsequent dynamical evolutionary phases.

Unified Astronomy Thesaurus concepts: Globular star clusters (656); Star clusters (1567); Blue straggler stars (168); Stellar populations (1622)

1. Introduction

Blue straggler stars (BSSs) are an exotic population of stars located in a more luminous and bluer region than main-sequence (MS) turn-off (TO) in the color–magnitude diagram (CMD) of stellar systems (e.g., Sandage 1953; Ferraro et al. 1997, 2003b, 2012, 2018; Piotto et al. 2004; Leigh et al. 2007; Boffin et al. 2015). They are core hydrogen-burning stars more massive (e.g., Fiorentino et al. 2014; Raso et al. 2019) than MS-TO objects and thought to be the outcome of two main processes: mass transfer and/or coalescence in binary systems (hereafter, MT-BSSs; McCrea 1964), and (2) direct stellar collisions (hereafter, COL-BSSs; Hills & Day 1976). Other processes, such as merger of close binary systems, possibly induced by Kozai–Lidov mechanisms in hierarchical triple systems, can also play a role in generating BSSs (Perets & Fabrycky 2009). While the formation channels requiring binary systems are common in all stellar environments and dominant in low-density conditions, such as the peripheries of globular clusters (GCs), open clusters, dwarf galaxies and the Galactic field, the collisional channel requires very-high-density environments. Hence, the inner cores of GCs offer the most favorable conditions for direct stellar collisions to occur, although the MT channel is considered the most prolific one (e.g., Davies et al. 2004; Knigge et al. 2009; Leigh et al. 2013). Since BSSs are ubiquitous and found in all GCs and are more massive than the average (e.g., Ferraro et al. 2018; Rain et al. 2021), they are used as powerful tools to study star cluster internal dynamics (e.g., Ferraro et al. 2012, 2018, 2019, 2020; Alessandrini et al. 2016; Lanzoni et al. 2016; Dresbach et al. 2022). In particular, Ferraro et al. (2018) studied about one-third of the entire GC population in our Galaxy and found a tight correlation between the number of relaxation times suffered by each cluster since formation ($N_{\rm relax}$) and the value of the $A^+_{\rm rh}$ parameter. The latter is defined as the area between the cumulative radial distribution of BSSs and that of a reference population (such as MS, giant, and horizontal branch stars), within a half-mass–radius from the center of the system (Alessandrini et al. 2016). Its value thus measures the level of BSS central segregation with respect to "standard" (lighter) stars, which progressively increases while the host cluster dynamically evolves. Large values of $A^+_{\rm rh}$ are therefore measured for GCs in late stages of their dynamical evolution, while small values (down to zero) are found in dynamically young systems, where dynamical friction has not been effective yet in segregating BSSs toward the center.

The distinction between BSSs formed through MT and collision would provide useful information about the collision rate of the cluster, the fraction of binaries and their impact on internal dynamics, and also insights into the formation and evolution of these exotic objects. Unfortunately, BSSs formed through different channels are hardly distinguishable from their photometric properties. The only exception known so far could be the presence of two distinct BSS sequences in the CMD of

post-core-collapse (PCC) clusters.[4] This feature was first discovered in the GC M30 (Ferraro et al. 2009), and it has since then been identified in a few additional systems: NGC 362 (Dalessandro et al. 2013), NGC 1261 (Simunovic et al. 2014; but see Raso et al. 2020), and M15 (Beccari et al. 2019).[5] A detection of a double BSS sequence in the Large Magellanic Cloud GC NGC 2173 has been claimed by Li et al. 2018, but this is most likely an artifact of field contamination (Dalessandro et al. 2019a, 2019b). All these clusters show in the CMD a narrow sequence of blue BSSs, separated through a clear-cut gap from a more scattered red BSS population. The red sparse sequence is not reproducible with collisional isochrones (Sills et al. 2009) of any age, while it is in good agreement with the CMD location of MT-BSS models (Xin et al. 2015), thus suggesting that it is likely populated by BSSs formed through the MT channel. On the other hand, the blue sequence is inconsistent with the MT-BSS models of Xin et al. (2015) and is well reproduced by collisional isochrones, thus suggesting that it is likely populated by COL-BSSs. Interestingly, Monte Carlo simulations by Jiang et al. (2017) show that the blue sequence could be also contaminated by MT-BSSs. However, its narrowness and the clear-cut separation from the red sequence appear to be inconsistent with a formation from MT activity in binary systems, which extends over long timescales. On the other hand, the results obtained by Jiang et al. (2017) could explain the presence of the few W-Uma stars (contact binaries) detected along the blue sequences of M30 and NGC 362 (Ferraro et al. 2009; Dalessandro et al. 2013). The narrowness of the blue sequence suggests that it is more likely composed of a population of coeval BSSs with different masses, all formed over a relatively short period of time. Based on this evidence, Ferraro et al. (2009) suggested that the origin of the observed blue sequence is related to the core-collapse (CC) event which enhanced the cluster collision rate in inner regions over a short timescale. This working hypothesis was later confirmed by numerical simulations specifically performed to reproduce the bimodal BSS distribution of M30 (see Portegies Zwart 2019). In addition, as a matter of fact, the three clusters where a double BSS sequence has been firmly identified so far (i.e., M30, NGC 362, and M15) already experienced the CC phase (see Harris 1996, 2010 edition). In light of all this, Ferraro et al. (2009) suggested that the properties of the blue narrow sequence could be also used to date back the CC epoch: as the MS-TO luminosity is a proxy of the cluster age, so the luminosity of the blue BSS sequence (or its extension in luminosity) can provide an estimate of the epoch when the system experienced a significant enhancement of its collision rate, which triggered the formation of COL-BSSs that we now observe aligned in the CMD.

In this paper we present the discovery of a double sequence of BSSs in the GC NGC 6256. This is a dense cluster ($\log \rho_0 \approx 5.9$ in units of $M_\odot$ pc^{-3}; Baumgardt & Hilker 2018) located in the Galactic bulge, at a distance of 6.8 kpc from the Sun (Cadelano et al. 2020b) and characterized by a relatively low metal content compared to typical bulge GCs ([Fe/H] $= -1.6$; Vasquez et al. 2018). In Cadelano et al. (2020b), we applied a well-tested procedure (see Pallanca et al. 2019, 2021) to quantify the differential reddening affecting the cluster, and we derived a high-resolution exctiction map (see Figure 3 in Cadelano et al. 2020b): color excess variations as large as $\delta E(B-V) \sim 0.51$ mag were measured in the relatively small $160'' \times 160''$ field of view (FOV) sampled by the adopted data set. The differential reddening-corrected CMD allowed the authors to derive an age of 13 ± 0.5 Gyr. The analysis of the CMD also revealed a severe contamination by field interlopers along the cluster's main evolutionary sequences.

In the comprehensive analysis of GC surface brightness profiles by Trager et al. (1993, 1995), NGC 6256 is classified as a PCC cluster, due to the presence of a central surface brightness cusp. However, cluster structural properties based on surface brightness profiles suffer from so-called "shot-noise bias", due to the stochastic and sparse presence of luminous stars, which can significantly displace the surface brightness peak from the true location of the cluster gravitational center and alter the shape of the surface brightness profile with respect to the true density distribution (see, e.g., Noyola & Gebhardt 2006; Cadelano et al. 2017; Lanzoni et al. 2019).

Recently, Cohen et al. (2021) determined the cluster's structural parameters from the star count density profile. They derived a cluster gravitational center by fitting ellipses to the isodensity contours, and found a value in agreement, within uncertanties, with the one quoted in Cadelano et al. (2020b), which was calculated through iterative recentering of the stellar average coordinates. They also determined the cluster's structural parameters through King (1966) model fitting of the density profiles obtained by combining the same high-resolution observations used throughout this work (see Section 2) to sample the central regions, with Gaia Data Release 2 photometry (Gaia Collaboration et al. 2018) to sample the cluster's outskirts. The authors discuss that the best-fit model is unable to properly reproduce the observed stellar density in the cluster's innermost regions, which is expected in the case of a very dynamically evolved and core-collapsed cluster.

This paper is structured as follows: in Section 2 we introduce the adopted data set and the data-reduction procedures; in Section 3 we determine the cluster's stellar density profile and investigate its dynamical status; in Section 4 we discuss the proper motion (PM) analysis and present the discovery of a double sequence of BSSs; finally, we summarize the results and draw our conclusions in Section 5.

2. Observations and Data Analysis

High-resolution data set. This work is mainly based on two data sets of optical images obtained with the Hubble Space Telescope (HST). The first data set was obtained using the UVIS channel of the Wide Field Camera 3 (WFC3) under GO 11628 (PI: Noyola). It consists of three images acquired with the F555W filter and an exposure time of 360 s, and three images in the F814W filter with an exposure time of 100 s. The adopted procedures of data reduction, astrometry, and calibration are described in detail in Cadelano et al. (2020b), where the determination of a high-resolution differential reddening map in the direction of the system is also discussed. The second data set was obtained under GO 15065 (PI: Cohen) using the Wide Field Camera (WFC) of the Advanced Camera for

[4] Core-collapse is a characteristic phase of the internal dynamical evolution of collisional stellar systems. It is the result of the continuous kinetic energy transfer from the inner regions to the outskirts that leads to a runaway contraction of the core, with a substantial increase of its density. PCC clusters are commonly recognized from the presence of steep power-law cups in the innermost portion of the density profile (Meylan & Heggie 1997).

[5] A detection of a double BSS sequence in the Large Magellanic Cloud GC NGC 2173 has been claimed by Li et al. (2018), but this is most likely an artifact of field star contamination (Dalessandro et al. 2019a, 2019b).

Surveys (ACS). It consists of four images acquired with the F606W filter with an exposure time of 498 s and four images acquired with the F814W filter with an exposure time of 509 s. The data reduction was performed using a standard approach with the DAOPHOT and ALLFRAME packages (Stetson 1987, 1994), in a similar way as described in Cadelano et al. (2020b) in the case of the WFC3 data set. The FOVs of the two HST data sets overlap and are separated by a temporal baseline of 3605 days (∼10 yr), thus allowing the measure of stellar PMs (see Section 4.1). All the HST magnitudes used hereafter throughout this work are corrected for the effects of differential reddening.

Wide-field data set. To dermine the stellar density profile along the entire radial extension of the cluster, we complemented the high-resolution HST data with a set of wide-field near-IR images obtained as a part of the VVVX survey (Minniti 2016). This data set was acquired with the VISTA InfraRed CAMera (VIRCAM) mounted on the VISTA-ESO telescope. It is composed of two images obtained with the *J* filter and an exposure time of 120 s, one image with the *H* filter and an exposure time of 48 s and, finally, one image with the *Ks* filter and an exposure time of 16 s. Also in this case, the data reduction was performed using a standard approach suitable for ground-based observations with the DAOPHOT and ALLFRAME packages (see, e.g., Cadelano et al. 2020a). The resulting catalog was astrometrized using the stars in common with the Gaia Data Release 3 (DR3) catalog (Gaia Collaboration 2022, in preparation) and the instrumental magnitudes were calibrated using the stars in common with the catalog by Valenti et al. (2007), obtained with the same filters and in an overlapping region of the sky.

A map of the FOVs covered by all the data sets used in this work is reported in Figure 1, while the corresponding CMDs are shown in Figure 2.

3. Stellar Density Profile and Structural Parameters

PCC clusters are typically characterized by the presence of a central density cusp usually shaped like a power law, rather than the flat density core behavior predicted by King (1966) models and typically observed in less dynamically evolved GCs (e.g., Ferraro et al. 2003a; Lanzoni et al. 2007; Vesperini & Trenti 2010; Dalessandro et al. 2013; Miocchi et al. 2013; Zocchi et al. 2016). Based on the shape of its surface density distribution, NGC 6256 has been classified as a PCC system (Trager et al. 1993, 1995). In this section, we determine the cluster's density profile from star counts to accurately estimate its structural properties and reliably confirm its core-collapsed nature.

We adopted the gravitational center derived in Cadelano et al. (2020b): $\alpha = 16^{\rm h}59^{\rm m}32\overset{\rm s}{.}668$ and $\delta = -37°07'15\overset{''}{.}139$, with an uncertainty of $\sim 0.4''$. As discussed in many previous papers (see Ferraro et al. 1999, 2003a; Ibata et al. 2009; Lanzoni et al. 2007) the accurate determination of the center of gravity is crucial in order to properly characterize the star density profile, especially in high-density clusters. The projected stellar density profile has been determined following the procedure fully described in Miocchi et al (2013; see also, e.g., Cadelano et al. 2017; Lanzoni et al. 2019; Raso et al. 2020). To sample the inner $\sim 100''$, we used the WFC3 data set. For the cluster's outer regions, we used the wide-field VIRCAM data set. The choice of using a near-IR data set, instead of the publicly available Gaia DR3 catalog, is motivated by the fact that NGC 6256 is located in a region of the sky severely affected by differential reddening (see Cadelano et al. 2020b). Hence, the adoption of a catalog of stars based on optical photometry, such as the Gaia one, could introduce significant alterations of the density profile with respect to its true shape, and thus lead to a wrong determination of the cluster structural parameters (see the case of M71 discussed in Cadelano et al. 2017).

In the case of the region sampled by the HST data set, we divided the FOV into 12 concentric annuli out to $120''$ from the cluster's center, each one divided into four subsectors. For each subsector, we then counted the number of stars with a magnitude $15.5 < m_{\rm F814W} < 19.8$ (to avoid possible biases due to saturation and incompleteness of the brightest and faintest stars, respectively) and divided it by the sampled area. The resulting density in each annulus is the mean of the values measured in each subsector and the uncertainty is the standard deviation. We repeated the same procedure for the VIRCAM wide-field data set, dividing the FOV into eight concentric annuli from $38''$ out to $450''$ from the cluster's center, and considering only stars with a magnitude $11.5 < K < 16.5$. The three innermost radial bins ($38'' < r < 120''$) are also sampled with the HST catalog, and thus they have been used to vertically rescale the external (VIRCAM) profile to match the inner (HST) one. The resulting density profile is shown in Figure 3 (empty circles). The apparent external flattening is due to the Galactic field contribution, which is negligible with respect to the cluster density in the inner regions, but becomes dominant at large distances from the center. The average of the three most external points in linear (instead of logarithmic) units has been adopted as Galactic field density, and then subtracted from the observed distribution to obtain the background-decontaminated density profile of NGC 6256 (filled circles in Figure 3). The density profile clearly shows a progressive increase, instead of a flat behavior, toward the cluster center, which is the typical feature expected for a core-collapsed GC.

The density profile has been obtained using only TO, subgiant, and red giant stars which approximately have the same mass. Therefore, the cluster's structural parameters have been derived by fitting the observed profile with a single-mass King (1966) model, assuming spherical symmetry and orbital isotropy. Following Raso et al. (2020), we performed the fit using a Markov Chain Monte Carlo approach by means of the emcee package (Foreman-Mackey et al. 2013, 2019). We assumed uniform priors on the parameters of the fit (i.e., the King concentration parameter c, the core radius r_c, and the value of the central density). Therefore, the posterior probability distribution functions are proportional to the likelihood $\mathscr{L} = \exp(-\chi^2/2)$, where the χ^2 statistic is calculated between the measured density values and those predicted by the whole family of adopted models. As typically found for core-collapsed GCs (e.g., Ferraro et al. 2003a; Zocchi et al. 2016), the resulting best-fit model (red dashed curve in the left-hand panel of Figure 3) clearly fails in properly reproducing the observations, and it is characterized by a value of the concentration parameter c larger than 2. Instead, a very good King model fitting is obtained if the three innermost points ($r < 5''$) are excluded from the analysis (red dashed curve in the right-hand panel of Figure 3). In turn, the evident central density cusp is well reproduced by a straight line, with a steep slope $\alpha_{\rm CUSP} = -0.89$ (red solid line in the figure). This is

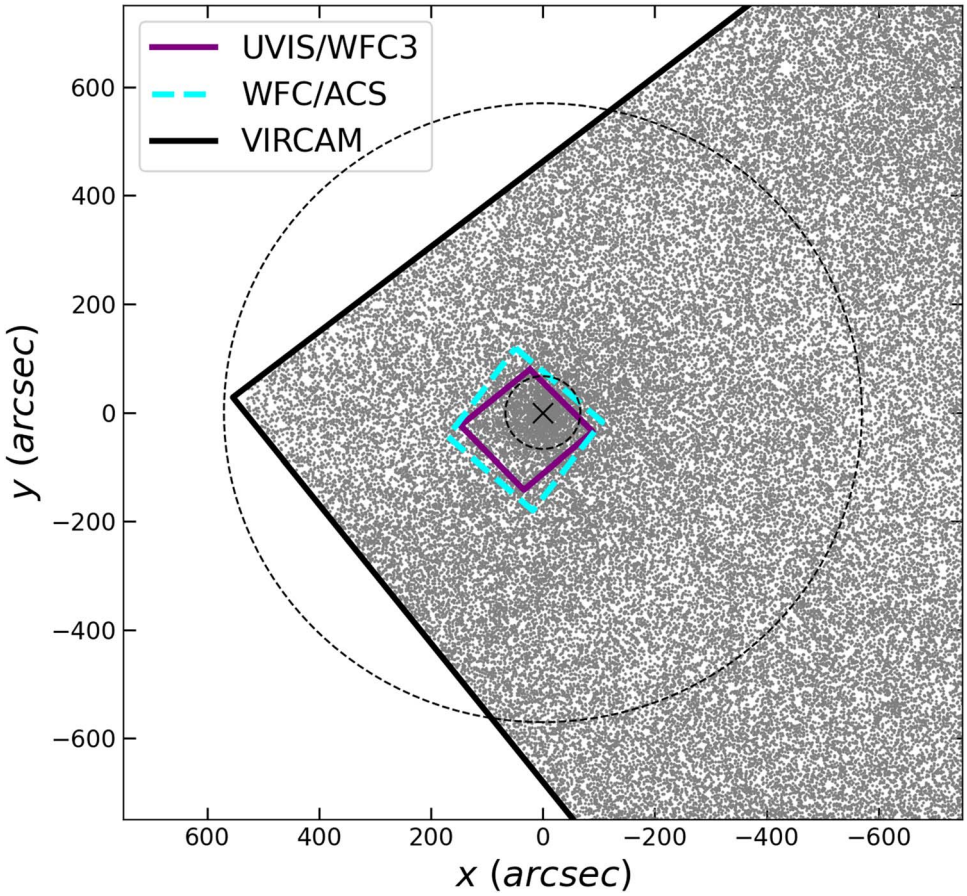

Figure 1. FOVs covered by the data sets used in this work, plotted with respect to the cluster's center (black cross) quoted in Cadelano et al. (2020b). The gray dots are the observed stars. The violet and cyan thick lines mark the FOVs of the WFC3 and ACS data sets, respectively. The black solid line marks the edge of a portion of the wide-field VIRCAM data set. The inner and outer dashed circles are the cluster's half-mass and tidal radii, respectively, as determined in Section 3.

indeed the typical behavior of a PCC cluster (e.g., Vesperini & Trenti 2010). The main structural parameters obtained from the best-fit King model are also labeled in the figures, where W_0 is the model dimensionless potential, $r_{\rm hm}$ is the three-dimensional half-mass–radius, and r_t is the truncation or tidal radius. Figure 4 compares the density profile obtained in this work (black circles) with that determined through a very similar procedure by Cohen et al. (2021, gray circles), vertically rescaled to match our data using an average density difference value. The two profiles are overall in good agreement, the main difference being that we sample a larger radial extension, both toward the center and in the periphery, with the density that keeps increasing in the innermost bin, as expected in the presence of a power-law cusp. This difference is likely due to different adoptions of the magnitude selection and slightly different coordinates of the cluster center. Nevertheless, the structural parameters derived here and in Cohen et al. (2021) are in agreement within $\sim 1-2\sigma$ errors.

4. The Blue Straggler Star Population and the A^+ Parameter

The shape of the density profile clearly indicates that NGC 6256 is in a very advanced stage of its dynamical evolution, having already experienced the CC phase. To independently and more quantitatively investigate the dynamical status of this system, we analyzed the properties of the BSS population, which are known to act as a "dynamical clock" (Ferraro et al. 2012, 2018, 2019; Lanzoni et al. 2016; Ferraro et al. 2020). However, NGC 6256 suffers from severe contamination from Galactic interlopers (Cadelano et al. 2020b), and a solid characterization of the BSS population first requires a proper distinction between the cluster's members and field objects. Unfortunately, due to crowding, large extinction, and distance, the kinematic information provided by the Gaia DR3 can be used only for the brightest portion of the red giant branch. Therefore, we took advantage of the large temporal baseline between the two HST data sets to perform PM analysis of the stars in common between the two epochs. A similar, independent analysis was also performed by Cohen et al. (2021).

4.1. Proper Motion Selection

We adopted the approach described in Dalessandro et al. (2013; see also Bellini et al. 2014; Cadelano et al. 2017; Dalessandro et al. 2018; Raso et al. 2020). The procedure consists of measuring the instrumental position displacements of the stars detected in both epochs, once a common distortion-free reference frame is defined. For each data set, we derived the mean instrumental positions (x,y) as the σ-clipped mean of the positions of stars detected in at least half the total number of images. In the WFC3 case, the resulting (x,y) positions have been corrected for geometric distortions by applying the equations published in Bellini et al. (2011). For the ACS catalog, we adopted the ACS/WFC Distortion Correction

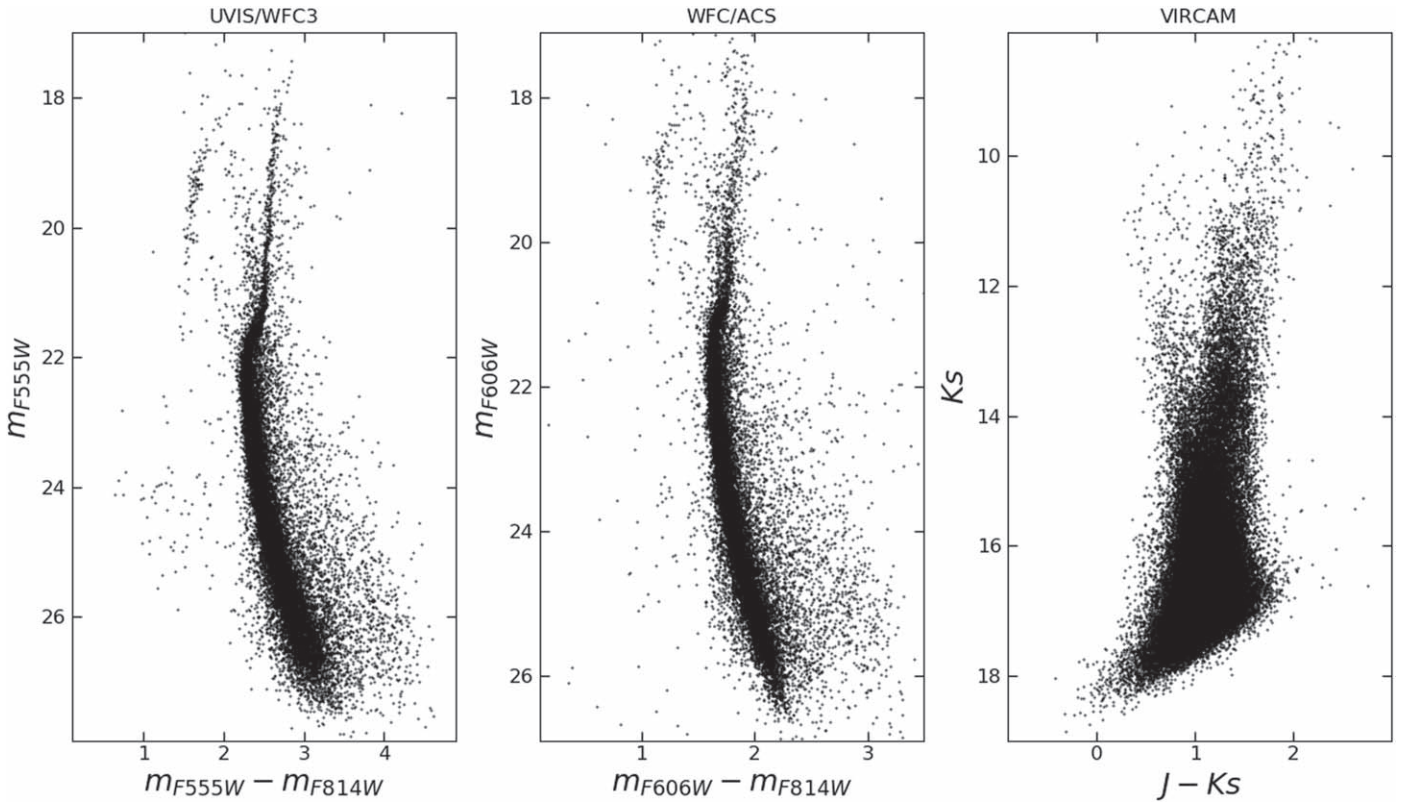

Figure 2. Left panel: ($m_{\rm F555W}$, $m_{\rm F555W} - m_{\rm F814W}$) CMD of NGC 6256 as obtained from the first epoch, WFC3 observations (from Cadelano et al. 2020b). Middle panel: ($m_{\rm F606W}$, $m_{\rm F606W} - m_{\rm F814W}$) CMD obtained from the second epoch, ACS observations. Both first- and second-epoch magnitudes are corrected for differential reddening. Right panel: (J, $J - Ks$) CMD of the cluster obtained from the VIRCAM observations.

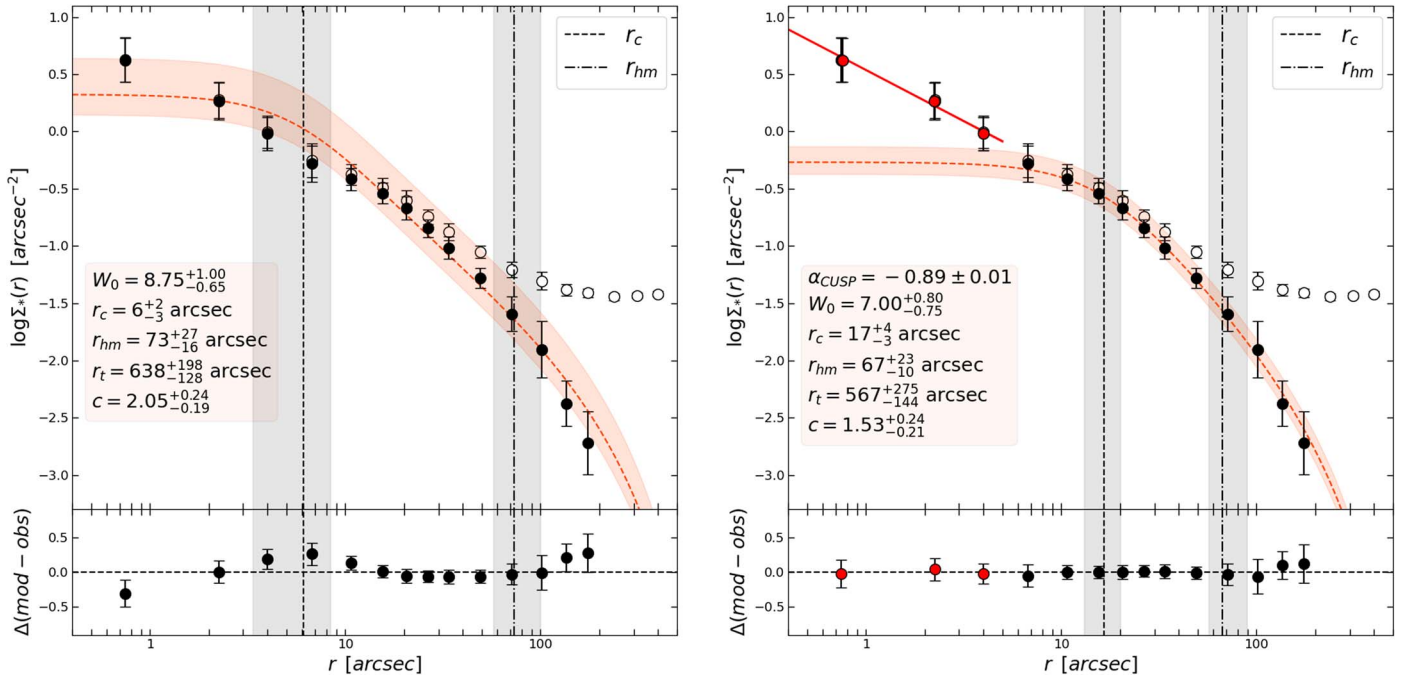

Figure 3. Left: observed (empty circles) and background-subtracted (filled circles) density profile of NGC 6256. The dashed red curve is the best-fit King model to the cluster density profile, and the red stripe marks the envelope of the $\pm 1\sigma$ solutions. The dashed and dotted–dashed vertical lines mark the best-fit cluster's core and half-mass radii, respectively, and their corresponding 1σ uncertainties are represented with the gray stripes. The best-fit values of some structural parameters (see text) are also labeled. The bottom panel shows the residuals between the best-fit King model and the cluster density profile. Right: same as in the left panel, but with the three innermost points colored in red to highlight the presence of a stellar density cusp. These points have been fitted with a power-law function, shown as a red solid line, having a slope $\alpha_{\rm CUSP}$ labeled in the figure legend. The best-fit King model to the profile obtained by excluding the three inner points (black solid circles) is shown with the red dashed curve and red stripe, and its corresponding parameters are labeled in the legend.

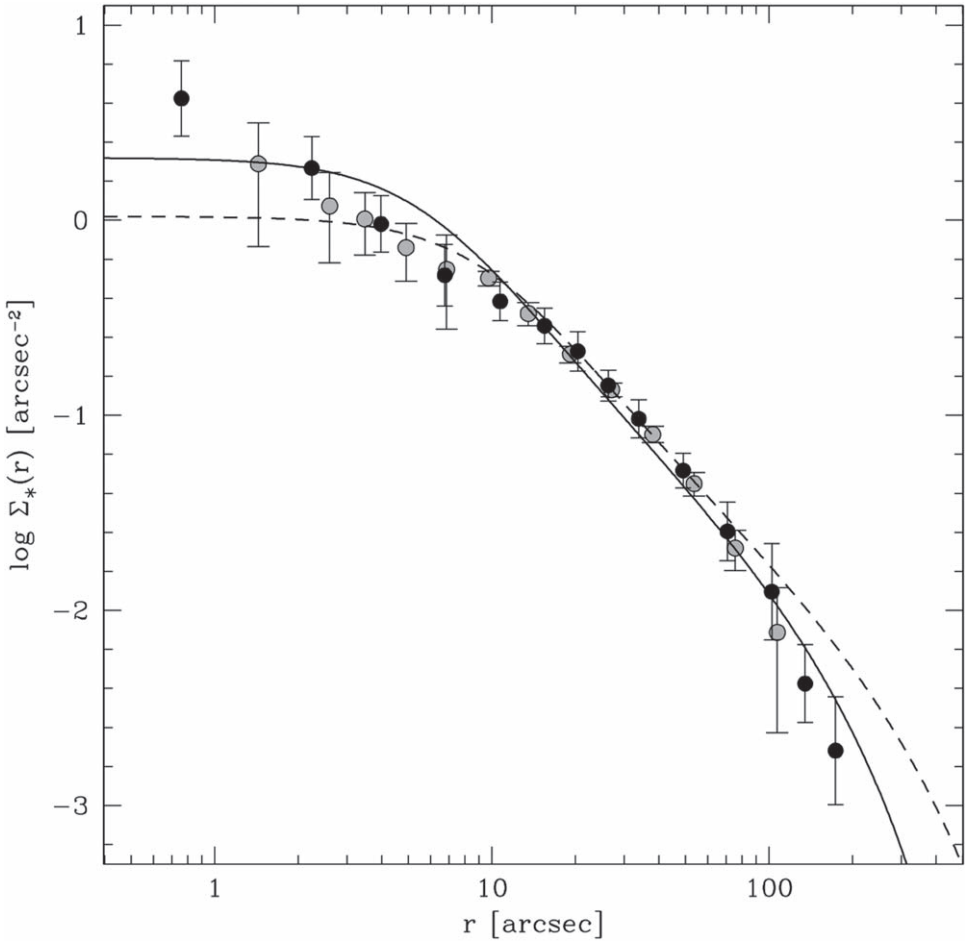

Figure 4. Comparison between the background-subtracted density profile of NGC 6256 determined in this work (black circles), and that obtained by Cohen et al. (2021), vertically rescaled to match the former (gray circles). The solid and dashed lines are, respectively, the best-fit King models determined here and in Cohen et al. (2021).

Tables (IDCTAB) provided in the dedicated page of the Space Telescope Science Institute. The latter catalog was adopted as a distortion-free reference frame, due to its slightly larger FOV. Then, we determined accurate transformations between the first-epoch WFC3 catalog and the reference frame. To this aim, we selected in both the catalogs a sample of stars that can be considered as likely cluster members on the basis of their CMD positions. We then applied a six-parameter linear transformation[6] to transform the positions of stars in the WFC3 frame to the reference frame, treating each chip independently in order to maximize the accuracy. The derived transformations have then been applied to all the stars in common between the two catalogs. The relative PMs are finally determined by measuring the difference of the mean (x,y) positions of each star in the two epochs, divided by their temporal baseline and multiplied by the pixel scale of the reference frame (50 mas pixel^{-1}). In such a way, the PMs along both the R.A. ($\mu_\alpha \cos\delta$) and the decl. (μ_δ) are expressed in units of mas yr^{-1}.

The resulting vector point diagram is shown in the left panel of Figure 5. To maximize the efficiency in removing field interlopers in the BSS region, we selected a sample of stars with $19.0 < m_{\rm F555W} < 22.5$ and evaluated their PM distributions along both the directions (see histograms in Figure 5). These distributions have been fitted with Gaussian functions centered on 0 and with standard deviation $\sigma \sim 0.21$ mas yr^{-1}. We selected as bona-fide cluster members those stars having a total PM smaller than the combined 2σ dispersion (i.e., 0.6 mas yr^{-1}). The resulting CMDs, showing separately clusters and field members after the PM selection, are shown in the two rightmost panels of Figure 5.

The decontamination of the CMD through PM selection successfully disentangles the cluster's population from the field one, thus opening the possibility to study in detail the properties of the BSSs population in the cluster's regions covered by the HST observations. To this purpose, we used the ACS photometry that provides the deepest and largest number of exposures, thus granting a significantly larger signal-to-noise ratio in the CMD region occupied by BSSs, with respect to what is achievable with the WFC3 data. The samples of 37 BSSs and 1585 reference stars used in the following analysis have been selected from the PM-cleaned CMD, as shown in Figure 6. To draw the BSS selection box, special care was devoted to separate this population from MS-TO and subgiant branch stars (SBG) and to avoid the inclusion of MS-TO star blends. To this end, we built the color histograms of the measured stars in different bins of magnitudes ∼0.2 wide, and we set the lower boundary of

[6] To do this, we used CataXcorr, a code developed by P. Montegriffo at the INAF Osservatorio di Astrofisica e Scienze dello Spazio di Bologna. This package is available at http://davide2.bo.astro. it/?paolo/Main/CataPack.html, and has been successfully used in a large number of papers by our group in past years.

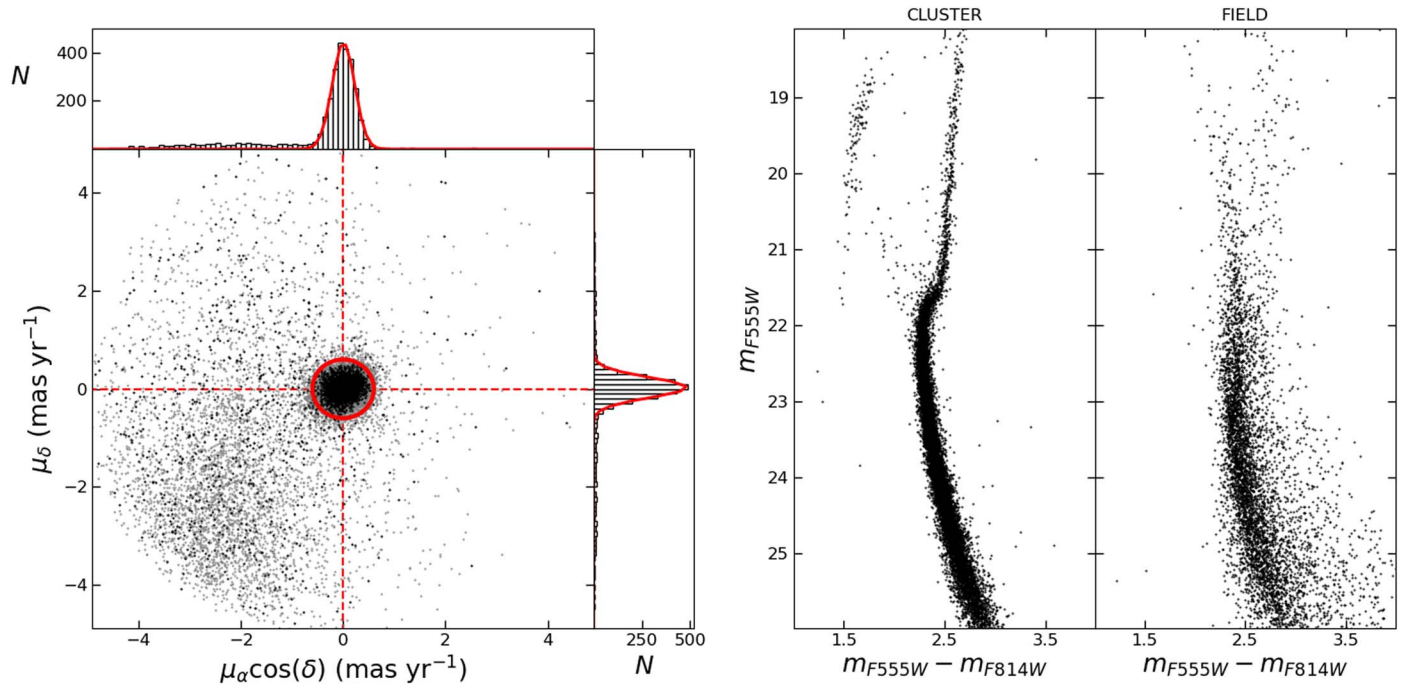

Figure 5. Left panel: vector point diagram of the stars in common between the two HST epochs, with the black dots being the subsample of stars with magnitude $19.0 < m_{\rm F555W} < 22.5$, and the gray dots corresponding to all the remaining stars. The upper and side plots show histograms of the PM distribution of the selected subsample along the R.A. and decl. directions, with superimposed the best-fit Gaussian function. The red circle in the main panel is centered on the mean values of the best-fit Gaussian functions (i.e., 0 mas yr^{-1}) and has a radius of 0.6 mas yr^{-1}, equal to the combined 2σ PM dispersion of the subsample (see text). This circle encloses all the stars that have been selected as bona-fide cluster members. Right panels: CMDs of the first-epoch data set for all the stars selected as cluster members (left) and for the stars selected as field interlopes (right).

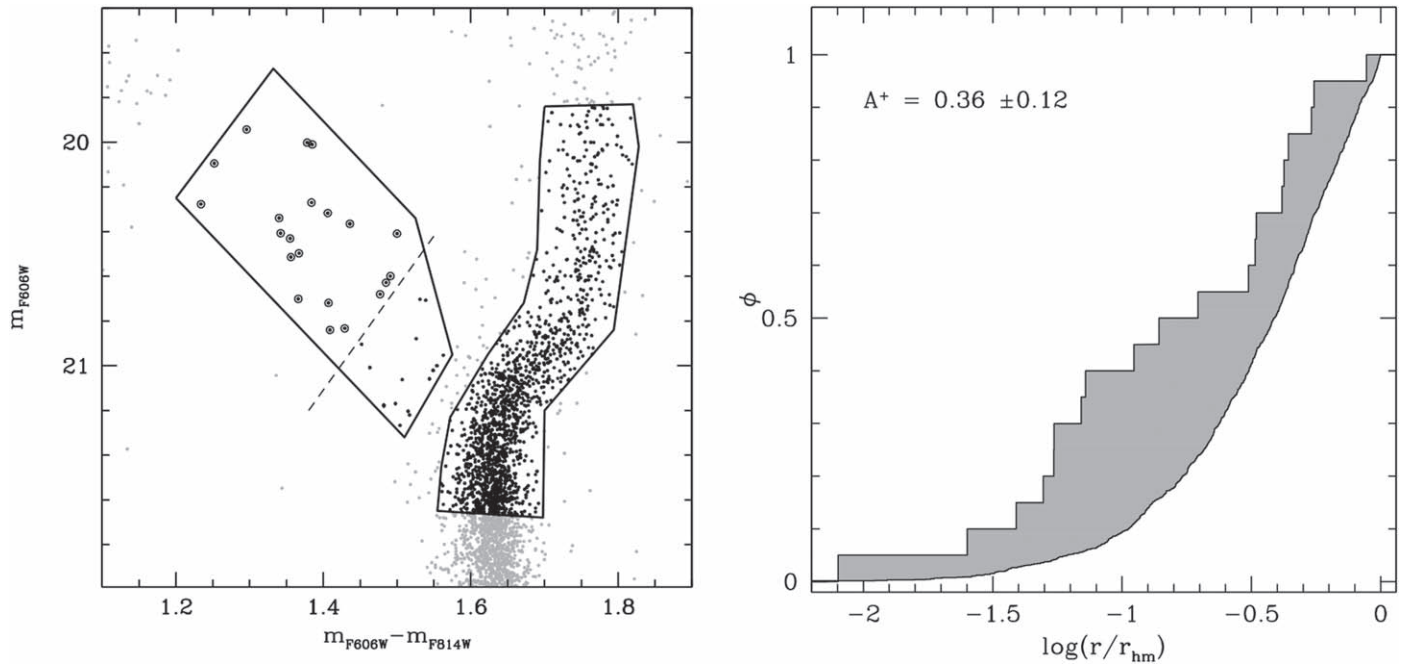

Figure 6. Left panel: PM-cleaned CMD of NGC 6256 (gray dots) with the selected populations of 37 BSSs and 1585 reference stars highlighted in black. The solid lines draw the adopted selection boxes. The dashed line marks the threshold used to select the bright BSS sample (empty circles) for the computation of A^+. Right panel: cumulative radial distributions of the 20 bright BSSs (upper line) and the 1368 reference stars (lower line) included with $r_{\rm hm}$, used to determine the A^+ parameter. The area of the region shaded in gray between the two cumulative radial distributions is the value of $A^+_{\rm rh}$, which is also labeled in the panel.

the BSS box at more than 4σ from the SBG distribution. The resulting box is similar to, but not coincident with, that of Leigh et al. (2011). Indeed, we adopted more conservative limits to avoid the inclusion of spurious objects, like (very bright) evolved BSSs and, especially, photometric blends of MS-TO stars. The reference population is composed of

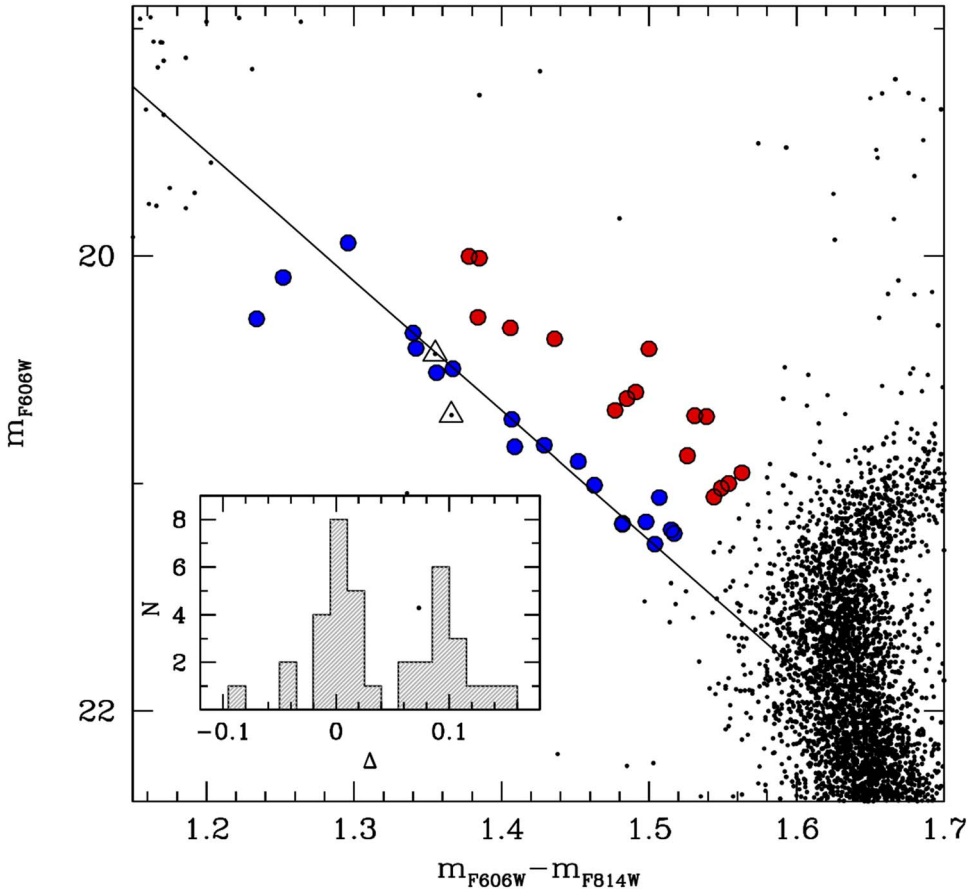

Figure 7. PM-selected CMD of NGC 6256 zoomed into the BSS region, with the BSSs aligned along the blue and the red sequence plotted as blue and red large circles, respectively. The empty triangles mark candidate variable stars. The black line is the linear fit to the blue BSS sequence (with slope 4.7 and intercept 14.04). The distribution of the BSS distances from this line is plotted as a histogram in the inset panel.

MS-TO, SGB and red giant branch stars in a magnitude range similar to that occupied by the BSSs.

4.2. A Double Sequence of Blue Straggler Stars

Figure 7 shows the cluster CMD zoomed in the BSS region. It is clearly populated by a narrow sequence of 21 BSSs on the bluer side, and by a more sparse population at redder colors, composed of 16 objects. It is worth mentioning that this result does not change if we apply different, less conservative PM selections. As a matter of fact, the double BSS sequence is clearly detected also in a CMD where no PM selection is applied at all (in that case, six more BSSs would be selected within the box in Figure 6, and they still align along the blue and red sequences). In order to quantitatively investigate the BSS distribution in the CMD, we measured the distance of each star from the best linear fit to the blue sequence (black line in the figure). A histogram of the BSS distances from this line is shown in the inset panel and it unambiguously reveals the presence of two well-defined peaks separated by ∼0.1 mag (i.e., almost one order of magnitude larger than the typical photometric color error in this magnitude range, which ranges between 0.014 and 0.016). Both the Akaike information criterion and the Bayesian information criterion tests (e.g., Hastie et al. 2001) confirm that the observed histogram is best reproduced by the sum of two Gaussian functions, with a probability larger than 99.5% that the distribution is bimodal, instead of unimodal. This is reminiscent of the behavior observed in other PCC clusters, where the narrow blue sequence has been interpreted as the evidence of a collisional population of BSSs (e.g., Ferraro et al. 2009; see also Section 1).

To verify whether this can be the case also for NGC 6256, we compared the observations with a set of collisional models of intermediate metallicity ([Fe/H] = −1.3) from the Sills et al. (2009) database. The collisional models adopt the Yale Rotational Evolutionary Code (Guenther et al. 1992) and were used to simulate and follow the evolution of a set of prototype BSSs formed by direct collisions between two MS isolated stars. In particular, 16 cases involving collisions of 0.4 $M_{\odot}$, 0.6 $M_{\odot}$, and 0.8 $M_{\odot}$ stars are investigated. Collisional products are generated using the code "Make Me A Star" (Lombardi, Jr et al. 2002) by assuming that the collision occurs with a periastron separation of 0.5 times the sum of the radii of the two stars. The evolution of collision products from the end of the collision to the MS phase is then traced following the prescription by Sills et al. (1997), and and it is stopped when the energy generation due to hydrogen burning is larger than that due to gravitational contraction, which corresponds to the zero-age MS. The subsequent evolution on the MS, giant, horizontal, and asymptotic giant branches is finally followed by using the Monash stellar evolution code for normal, low-mass stars (Karakas et al. 2002). Two collisional isochrones (at 0.1 and 1 Gyr) have been determined from the evolutionary tracks of three collision events involving stars with different masses (0.6 $M_{\odot}$ + 0.8 $M_{\odot}$, 0.6 $M_{\odot}$ + 0.6 $M_{\odot}$, and 0.5 $M_{\odot}$ +

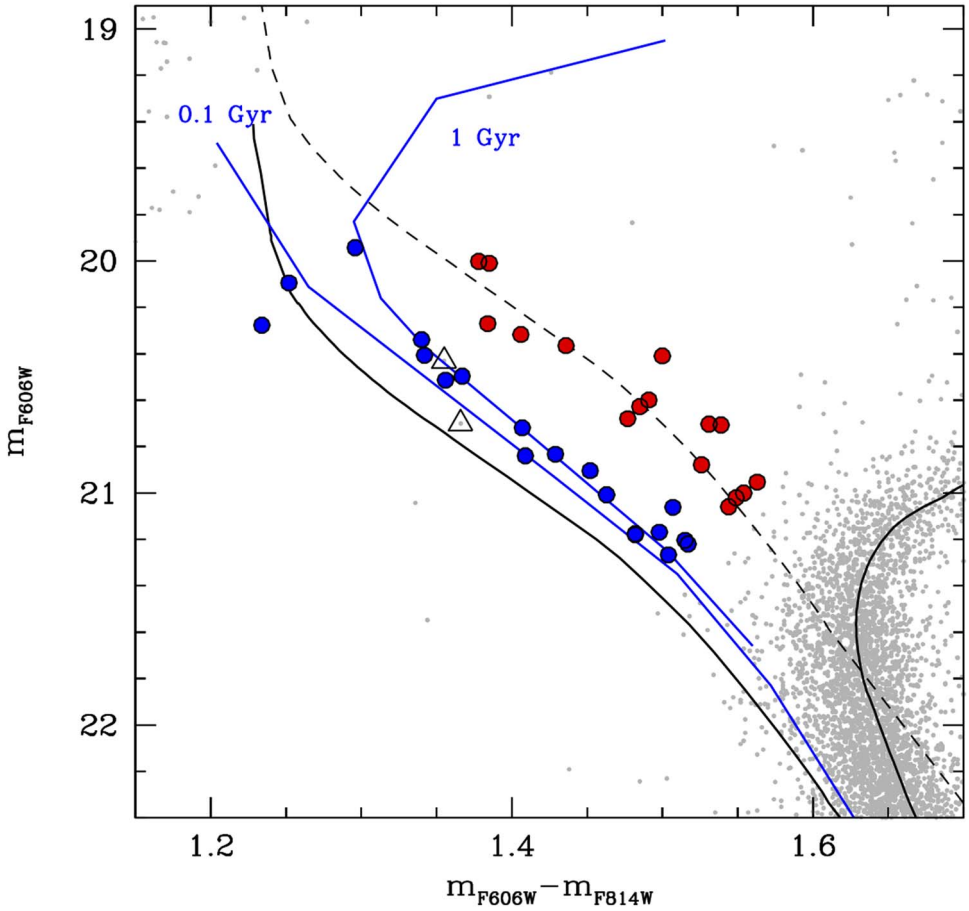

Figure 8. As in Figure 7, but with models superposed. The two thick blue lines correspond to collisional isochrones (Sills et al. 2009) of 0.1 and 1 Gyr (see labels) and they well repoduce the observed BSS blue sequence. The black solid lines are standard isochrones extracted from the Dotter et al. (2008) database and computed for the cluster metallicity ([Fe/H]= −1.6) at 1 and 13 Gyr (leftmost and rightmost curves, respectively). The black dashed line corresponds to the 1 Gyr isochrone shifted in magnitude by = −0.75.

0.6 $M_{\odot}$), and they are shown as blue curves in Figure 8. The matching with the blue BSS sequence is impressive: the position of the vast majority of the BSSs observed on the blue side of the CMD is very nicely reproduced by the 1-Gyr-old collisional isochrone. NGC 6256 is therefore the fourth PCC cluster where a sequence of collisional BSSs is clearly identified. The dashed line in the figure (corresponding approximately to the zero-age MS shifted by −0.75 magnitudes) traces the locus occupied by (unresolved) equal-mass binary systems and it well corresponds to the CMD position of the red BSS sequence. According to the scenario depicted in Section 1, BSSs belonging to the blue sequence are mostly formed through collisions in a recent and short-lasting event (the cluster CC), while those belonging to the red sequence are likely formed through MT in binary systems.

The CMD region occupied by BSSs can be populated by variable stars (e.g., Rodríguez & López-González 2000; Dieball et al. 2007; Beccari et al. 2019), with the optical variability due either to pulsations (as in the case of SX Phoenicis), or to binarity (e.g., cataclysmic variables and W-Uma). To verify whether some of the selected BSSs belong to these categories, we first inspected the Catalogue of Variable Stars in GCs by Clement et al. (2001). This lists a bright pulsating variable (see also Matsunaga et al. 2006) in the direction of NGC 6256, with a mean K-band magnitude of 10.85, which is however saturated in our exposures. We also verified there are no common stars among our BSSs catalog and the GAIA DR3 catalog, which provides a flag for stars displaying photometric variability. The lack of BSSs in common with Gaia is not surprising and is due to limited performances of the satellite in the crowded and highly extincted environment of this cluster. Finally, we carefully investigated the possible presence of optical variability along the BSS sequence by analyzing the single frame magnitudes obtained from our photometric analysis. Two stars show significant magnitude variations due to intrinsic variability rather than photometric errors. They both lie along the blue sequence (empty triangles in Figure 8), where BSSs formed though collisions (hence, not belonging to binary systems) are expected. However, to confirm the variability of these objects and shed light on its nature (pulsation or binarity) a larger number of observations able to properly sample the light curve is needed. In any case, a very small contamination of the blue (collisional) sequence from variable binary stars has been already observed in other clusters. For example, one W-Uma variable has been identified along the blue BSS sequence in both M30 (Ferraro et al. 2009) and NGC 362 (Dalessandro et al. 2013).

No statistically significant difference is found between the cumulative radial distributions of the blue and the red sequences. Conversely, the red BSS population was found to be more centrally segregated than the blue one in the other investigated GCs, with a large (3σ) significance only in the case

of NGC 362 (Dalessandro et al. 2013), where the samples are the most numerous. This finding could therefore be due just to an effect of small statistics, or it could hide some clues about the formation of these objects. More similar investigations in a larger sample of GCs are needed to clarify this issue and properly address the physical origin of the possible difference in the radial segregation of the two BSS populations.

4.3. Measuring the Dynamical Age from the "Dynamical Clock"

To further investigate the dynamical status of NGC 6256, we applied the so-called "dynamical clock": an empirical measurement of the cluster dynamical evolution level based on the observational properties of the BSS (Ferraro et al. 2012, 2018). In particular, following Lanzoni et al. (2016) and Ferraro et al. (2018, 2020), we measured the segregation level of the BSS as determined by the value of the $A^+_{\rm rh}$ parameter, defined by Alessandrini et al. (2016) as the area between the cumulative radial distributions of BSSs and reference stars selected within one half-mass–radius from the center. For a proper comparison with previous results obtained for around one-third of the entire Galactic GC population (Ferraro et al. 2018), we selected only the brighter portion of the BSS population (i.e., the stars above the dashed line shown in the left panel of Figure 6). We adopted the half-mass–radius derived from the best fit with a King model of the entire density profile ($r_{\rm hm} = 73''$; left panel of Figure 3). Although this value and that obtained excluding the innermost $5''$ from the fit are in agreement within uncertainties, the former, in spite of a poorer fit to the observations, better corresponds to the true distance from the center that includes half of the total cluster mass (see right panel of Figure 3). The right panel of Figure 6 shows the cumulative radial distributions of the 20 BSSs and 1368 reference stars (upper and lower black lines, respectively) selected within the half-mass–radius. As expected for dynamically evolved GCs, the BSS distribution is clearly more centrally concentrated than the reference sample. Indeed, Kolmogorov–Smirnoff and the Anderson–Darling tests return a probability of 0.008 and 0.001, respectively, that the two samples are extracted from the same parent distribution.

The area between the two cumulative distributions shown in Figure 6 is shaded in gray and corresponds to $A^+_{\rm rh} = 0.36 \pm 0.12$. Since the main source of uncertainty is the small number statistics of the BSS population, the error has been estimated through a jackknife bootstrapping technique (Lupton 1993; see also Dalessandro et al. 2019c), recalculating the area between the cumulative distributions $N_{\rm BSS}$ times (where $N_{\rm BSS} = 20$ is the number of BSSs), excluding during each iteration one star from the sample. The obtained value of $A^+_{\rm rh}$ is among the largest determined so far (see Ferraro et al. 2018) for Galactic GCs. This is fully consistent with the classification of NGC 6256 as a PCC cluster. It is worth mentioning that, as shown in Figure 1, the available HST data uniformly samples about ∼84% of the cluster region within one half-mass–radius; the remaining ∼16% is outside the FOV beyond the edges of the ACS camera. This could lead to a slight underestimate of the $A^+_{\rm rh}$ value. With this caveat in mind, we compared the position of NGC 6256 in the $A^+_{\rm rh}$ versus $N_{\rm relax}$ diagram, together with the 48 Galactic GCs already investigated by Ferraro et al. (2018). As in previous studies, $N_{\rm relax}$ is defined as the ratio between the typical GC age (12 Gyr) and the central relaxation time ($t_{\rm rc}$) of each system. This is usually estimated from Equation (10) in Djorgovski (1993), which is appropriate for stellar systems well described by the King model family. Although this is not the case for NGC 6256 (see Section 3), we still adopted the same approach, assuming as concentration parameter and core radius the values obtained from the fit to the entire density profile (left panel in Figure 3). We adopted a central surface brightness $\mu_0 = 18.36$, directly measured from the F555W images within $1''$ from the center. This value has been corrected for the effect of extinction using an average color excess of $E(B-V) = 1.34$, estimated from the reddening map of Cadelano et al. (2020b) within the same sky area. We also adopted a distance $d = 6.8$ kpc (Cadelano et al. 2020b), an absolute magnitude $M_V = -7.15$ (Harris 1996, 2010 edition), an average stellar mass of 0.3 $M_\odot$, and a mass-to-light ratio of 2 (which are typical values for a ∼13 Gyr old GC; e.g., Maraston 1998). The resulting value of the central relaxation time is $\log(t_{\rm rc}) = 7.06$ (expressed in years), indicating that the cluster experienced more than one thousand current relaxation times since its formation, corresponding to $\log(N_{\rm relax}) = 3.02$. The position of NGC 6256 in the $A^+_{\rm rh}$ versus $N_{\rm relax}$ diagram is highlighted as a red diamond in Figure 9. Its position is in very good agreement with the trend drawn by the Galactic GC population and confirms that NGC 6256 is in a very advanced stage of its dynamical evolution. Indeed, it lies in the same region of the diagram occupied by the other PCC clusters of the sample, and its inclusion negligibly modifies the coefficients of the best-fit line. All this further demonstrates that $A^+_{\rm rh}$ is a powerful indicator of the degree of dynamical evolution of GCs.

5. Summary and Conclusions

In this paper we have performed a detailed photometric investigation of the bulge GC NGC 6256, also taking advantage of HST multiepoch data to measure relative PMs in the inner region of the system for the accurate decontamination of the CMD from field stars. The analysis demonstrated that this GC is in a very advanced stage of dynamical evolution. In fact, the observed stellar density profile cannot be properly reproduced by a King model, and shows a steep power-law cusp with a slope of −0.89 in the innermost ∼5″. This is the typical behavior expected for a cluster that already experienced CC (see, e.g., Bhat et al. 2022). A very advanced dynamical stage is also suggested by the value of the A^+ parameter (Alessandrini et al. 2016), measuring the level of BSS central segregation, with respect to lighter (MS-TO and giant) stars. As shown in Figure 9, NGC 6256 well follows the same trend between A^+ and $N_{\rm relax}$ traced by around one-third of the entire Galactic GC population (from Ferraro et al. 2018), and it locates in the region of the diagram occupied by PCC clusters (diamonds).

The analysis also showed that the BSS population of NGC 6256 draws a well-defined narrow blue sequence (corresponding to what is expected for a subpopulation of BSSs with different masses generated over a relatively short timescale), and a more sparse red sequence. This is similar to that observed in other PCC clusters (M30, NGC 362, and M15), where it has been interpreted (e.g., Ferraro et al. 2009) as the manifestation of the two main BSS formation channels: the blue sequence should be originated mainly by collisions over a short timescale, while the red sequence derives from a continuous formation process (see also Portegies Zwart 2019), as expected in the case of MT-generated BSSs. Indeed, the comparison with collisional models from Sills et al. (2009) computed for a metallicity appropriate for NGC 6256 provides a very good match to the observations: the narrow blue sequence is well

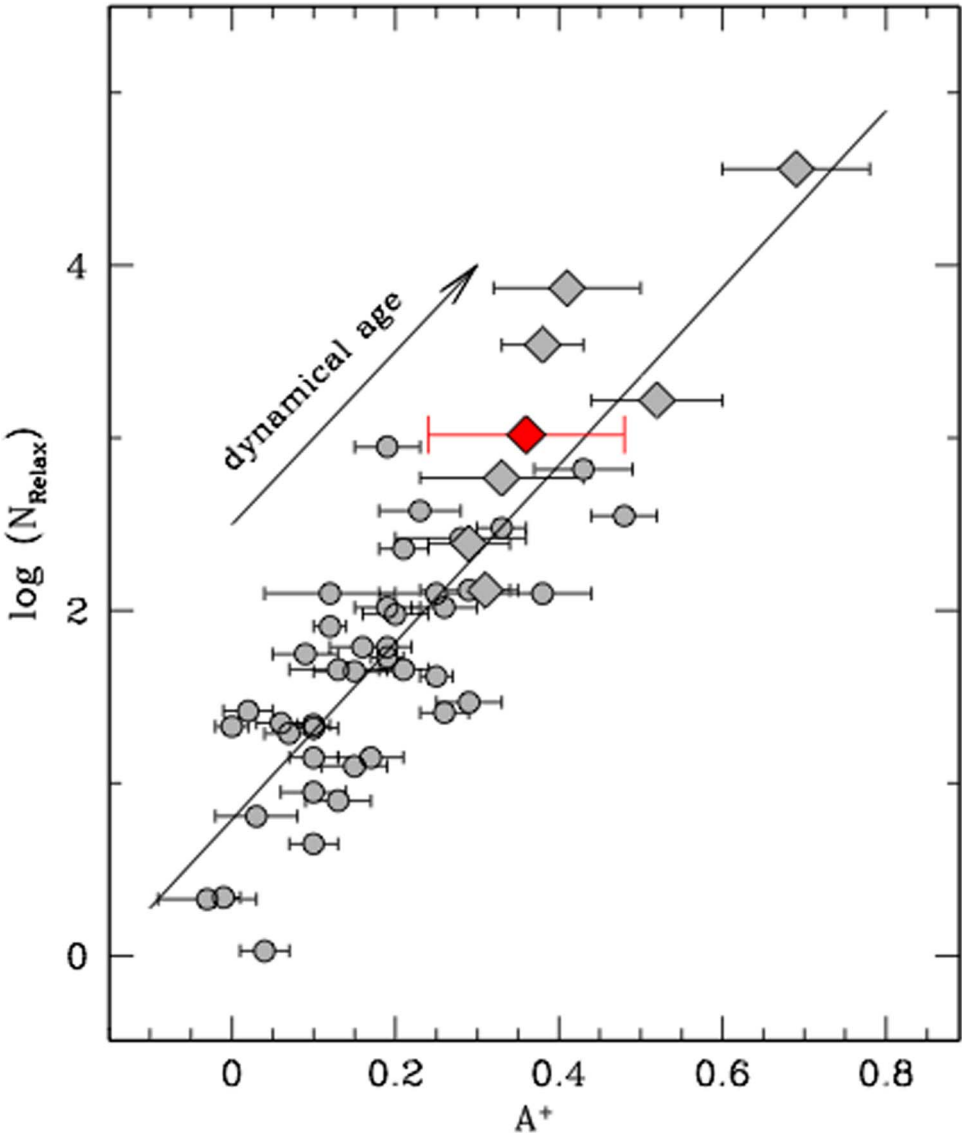

Figure 9. Relation between A^+ and $\log(N_{\rm relax})$ (solid line) obtained by Ferraro et al. (2018) for 48 Galactic GCs (gray symbols; circles and diamonds mark "normal" and PCC clusters, respectively). The position of NGC 6256 is marked with a red diamond.

reproduced by a collisional isochrone of 1 Gyr, thus suggesting that, approximately 1 Gyr ago, a short-lasting event occurred and promoted the formation of a population of collisional BSSs, which currently represents ∼60% of the entire BSS cluster content. The fact that NGC 6256 is a PCC system naturally yields to the conclusion that the blue sequence was originated by the increased collision rate during the CC phase. Based on analogous considerations, Ferraro et al. (2018) and Dalessandro et al. (2013) concluded that M30 experienced CC approximately 2 Gyr ago, and NGC 362 reached this phase of dynamical evolution more recently, about 0.2 Gyr ago. In the case of M15, the blue sequence is further separated in two different branches: the main one extends up to 2.5 mag above the MS-TO and is nicely reproduced by a ∼2.2 Gyr collisional isochrone, while the second is ∼1 mag less extended in the CMD and reproduced by a ∼5.5 Gyr collisional isochrone (Beccari et al. 2019). The authors suggest that such a complex feature could be the result of two distinct events of high collisional activity: the first one is the cluster CC, which occurred about 5.5 Gyr ago, and the second and more recent one corresponds to a core oscillation during the PCC evolution (see Figure 9 in Beccari et al. 2019). Intriguingly, the CMD positions of the two brightest BSSs along the blue sequence of NGC 6256 are consistent with a 0.1 Gyr collisional isochrone, thus possibly indicating the epoch of the last relevant recollapse during the PCC gravothermal oscillation phase, similarly to the case of M15.

Of course, the photometric separation of the two kinds of BSSs in the CMD is not completely stringent. In fact, while MT-BSSs are unable to produce blue sequences as narrow and well defined as observed, recent MT models (Jiang et al. 2017) demonstrate that some of them can "contaminate" the blue region of the CMD. This is indeed consistent with the presence of W-Uma variables identified along the blue sequence of M30 (Ferraro et al. 2009) and NGC 362 (Dalessandro et al. 2013), and possibly also in NGC 6256, where hints of photometric variability have been found for two blue BSSs (see Figure 8). On the other hand, collisional BSSs that were born along the blue sequence also cross the red sequence region during their natural evolution. However, the possibility of observing a

collisional BSS during its evolution through the red portion of the CMD is low (for instance, a 1.1 $M_{\odot}$ collisional BSS originated by a 0.5 $M_{\odot} + 0.6$ $M_{\odot}$ collision spends approximately 2 Gyr along the blue sequence, and only a few 10^8 yr crossing the red strip).

The analysis discussed in this paper for NGC 6256, together with previous results for other PCC and "normal" GCs (e.g., Ferraro et al. 2009, 2018; Dalessandro et al. 2013; Beccari et al. 2019), provide excellent examples of the potential prediction power of the BSS distribution in tracing the dynamical history of stellar systems. The segregation level of BSSs is a very powerful empirical way for the classification of GCs in terms of their level of internal dynamical evolution. Further, the morphology of the BSS sequence in the CMD can be used to trace the timescale of dynamical evolution during and after CC.

We thank the anonymous referee for their comments and suggestions that improved the quality of the manuscript. We warmly thank Alison Sills for providing us the collision isochrones used in this work. This work is part of the project Cosmic-Lab at the Physics and Astronomy Department "A. Righi" of the Bologna University (http://www.cosmic-lab.eu/ Cosmic-Lab/Home.html). This research was funded by the MIUR through a PRIN-2017 grant awarded to the project Light-on-Dark (PI: Ferraro) through contract PRIN-2017K7REXT.

ORCID iDs

Mario Cadelano https://orcid.org/0000-0002-5038-3914
Francesco R. Ferraro https://orcid.org/0000-0002-2165-8528
Emanuele Dalessandro https://orcid.org/0000-0003-4237-4601
Barbara Lanzoni https://orcid.org/0000-0001-5613-4938
Cristina Pallanca https://orcid.org/0000-0002-7104-2107
Sara Saracino https://orcid.org/0000-0003-4746-6003

References

Alessandrini, E., Lanzoni, B., Ferraro, F. R., Miocchi, P., & Vesperini, E. 2016, ApJ, 833, 252
Baumgardt, H., & Hilker, M. 2018, MNRAS, 478, 1520
Beccari, G., Ferraro, F. R., Dalessandro, E., et al. 2019, ApJ, 876, 87
Bellini, A., Anderson, J., & Bedin, L. R. 2011, PASP, 123, 622
Bellini, A., Anderson, J., van der Marel, R. P., et al. 2014, ApJ, 797, 115
Bhat, B., Lanzoni, B., Ferraro, F. R., & Vesperini, E. 2022, ApJ, 926, 118
Boffin, H. M. J., Carraro, G., & Beccari, G. 2015, Ecology of Blue Straggler Stars, Vol. 413 (Berlin: Springer)
Cadelano, M., Dalessandro, E., Ferraro, F. R., et al. 2017, ApJ, 836, 170
Cadelano, M., Dalessandro, E., Webb, J. J., et al. 2020a, MNRAS, 499, 2390
Cadelano, M., Saracino, S., Dalessandro, E., et al. 2020b, ApJ, 895, 54
Clement, C. M., Muzzin, Adam, Dufton, Quentin, et al. 2001, AJ, 122, 2587
Cohen, R. E., Bellini, A., Libralato, M., et al. 2021, AJ, 161, 41
Dalessandro, E., Cadelano, M., Vesperini, E., et al. 2019c, ApJL, 884, L24
Dalessandro, E., Ferraro, F. R., Bastian, N., et al. 2019a, A&A, 621, A45
Dalessandro, E., Ferraro, F. R., Bastian, N., et al. 2019b, RNAAS, 3, 38
Dalessandro, E., Ferraro, F. R., Massari, D., et al. 2013, ApJ, 778, 135
Dalessandro, E., Lardo, C., Cadelano, M., et al. 2018, A&A, 618, A131
Davies, M. B., Piotto, G., & Angeli, F. de 2004, MNRAS, 349, 129
Dieball, A., Knigge, C., Zurek, D. R., et al. 2007, ApJ, 670, 379
Djorgovski, S. 1993, in ASP Conf. Ser. 50, Structure and Dynamics of Globular Clusters, ed. S. G. Djorgovski & G. Meylan (San Francisco, CA: ASP), 373
Dotter, A., Chaboyer, B., Jevremovic, D., et al. 2008, ApJS, 178, 89
Dresbach, F., Massari, D., Lanzoni, B., et al. 2022, ApJ, 928, 47
Ferraro, F. R., Beccari, G., Dalessandro, E., et al. 2009, Natur, 462, 1028
Ferraro, F. R., Lanzoni, B., Dalessandro, E., et al. 2012, Natur, 492, 393
Ferraro, F. R., Lanzoni, B., Dalessandro, E., et al. 2019, NatAs, 3, 1149
Ferraro, F. R., Lanzoni, B., Raso, S., et al. 2018, ApJ, 860, 36
Ferraro, F. R., Paltrinieri, B., Fusi Pecci, F., et al. 1997, A&A, 324, 915, arXiv: astro-ph/9703026
Ferraro, F. R., Possenti, A., Sabbi, E., et al. 2003a, ApJ, 595, 179
Ferraro, F. R., Lanzoni, B., & Dalessandro, E. 2020, RLSFN, 31, 19
Ferraro, F. R., Paltrinieri, B., Rood, R. T., & Dorman, B. 1999, ApJ, 522, 983
Ferraro, F. R., Sills, A., Rood, R. T., Paltrinieri, B., & Buonanno, R. 2003b, ApJ, 588, 464
Fiorentino, G., Lanzoni, B., Dalessandro, E., et al. 2014, ApJ, 783, 34
Foreman-Mackey, D., Conley, A., Meierjurgen Farr, W., et al. 2013, emcee: The MCMC Hammer, Astrophysics Source Code Library, ascl:1303.002
Foreman-Mackey, D., Farr, W., Sinha, M., et al. 2019, JOSS, 4, 1864
Gaia Collaboration, Brown, A. G. A., Vallenari, A., et al. 2018, A&A, 616, A1
Guenther, D. B., Demarque, P., Kim, Y.-C., & Pinsonneault, M. H. 1992, ApJ, 387, 372
Harris, W. E. 1996, AJ, 112, 1487
Hastie, T., Friedman, J., & Tibshirani, R. 2001, The Elements of Statistical Learning, Springer Series in Statistics (New York: Springer)
Hills, J. G., & Day, C. A. 1976, ApL, 17, 87
Ibata, R., Bellazzini, M., Chapman, S. C., et al. 2009, ApJL, 699, L169
Jiang, D., Chen, X., Li, L., & Han, Z. 2017, ApJ, 849, 100
Karakas, A. I., Lattanzio, J. C., & Pols, O. R. 2002, PASA, 19, 515
King, I. R. 1966, AJ, 71, 64
Knigge, C., Leigh, N., & Sills, A. 2009, Natur, 457, 288
Lanzoni, B., Dalessandro, E., Ferraro, F. R., et al. 2007, ApJL, 668, L139
Lanzoni, B., Ferraro, F. R., Alessandrini, E., et al. 2016, ApJL, 833, L29
Lanzoni, B., Ferraro, F. R., Dalessandro, E., et al. 2019, ApJ, 887, 176
Leigh, N., Knigge, C., Sills, A., et al. 2013, MNRAS, 428, 897
Leigh, N., Sills, A., & Knigge, C. 2007, ApJ, 661, 210
Leigh, N., Sills, A., & Knigge, C. 2011, MNRAS, 415, 3771
Li, C., Deng, L., Grijs, R. de, Jiang, D., & Xin, Y. 2018, ApJ, 856, 25
Lombardi, Jr, J. C., Warren, J. S., Rasio, F. A., Sills, A., & Warren, A. R. 2002, ApJ, 568, 939
Lupton, R. 1993, Statistics in Theory and Practice (Princeton, NJ: Princeton Univ. Press)
Maraston, C. 1998, MNRAS, 300, 872
Matsunaga, N., Fukushi, H., Nakada, Y., et al. 2006, MNRAS, 370, 1979
McCrea, W. H. 1964, MNRAS, 128, 147
Meylan, G., & Heggie, D. C. 1997, A&ARv, 8, 1
Minniti, D. 2016, Galactic Surveys: New Results on Formation, Evolution, Structure and Chemical Evolution of the Milky Way, Vol. 10
Miocchi, P., Lanzoni, B., Ferraro, F. R., et al. 2013, ApJ, 774, 151
Noyola, E., & Gebhardt, K. 2006, AJ, 132, 447
Pallanca, C., Ferraro, F. R., Lanzoni, B., et al. 2019, ApJ, 882, 159
Pallanca, C., Ferraro, F. R., Lanzoni, B., et al. 2021, ApJ, 917, 92
Perets, H. B., & Fabrycky, D. C. 2009, ApJ, 697, 1048
Piotto, G., De Angeli, F., King, I. R., et al. 2004, ApJL, 604, L109
Portegies Zwart, S. 2019, A&A, 621, L10
Rain, M. J., Ahumada, J. A., & Carraro, G. 2021, A&A, 650, A67
Raso, S., Libralato, M., Bellini, A., et al. 2020, ApJ, 895, 15
Raso, S., Pallanca, C., Ferraro, F. R., et al. 2019, ApJ, 879, 56
Rodríguez, E., & López-González, M. J. 2000, A&A, 359, 597
Sandage, A. R. 1953, AJ, 58, 61
Sills, A., Karakas, A., & Lattanzio, J. 2009, ApJ, 692, 1411
Sills, A., Lombardi, James C. J., Bailyn, C. D., et al. 1997, ApJ, 487, 290
Simunovic, M., Puzia, T. H., & Sills, A. 2014, ApJL, 795, L10
Stetson, P. B. 1987, PASP, 99, 191
Stetson, P. B. 1994, PASP, 106, 250
Trager, S. C., Djorgovski, S., & King, I. R. 1993, in ASP Conf. Ser. 50, Structure and Dynamics of Globular Clusters, ed. S. G. Djorgovski & G. Meylan (San Francisco, CA: ASP), 347
Trager, S. C., King, I. R., & Djorgovski, S. 1995, AJ, 109, 218
Valenti, E., Ferraro, F. R., & Origlia, L. 2007, AJ, 133, 1287
Vasquez, S., Saviane, I., Held, E. V., et al. 2018, A&A, 619, A13
Vesperini, E., & Trenti, M. 2010, ApJL, 720, L179
Xin, Y., Ferraro, F. R., Lu, P., et al. 2015, ApJ, 801, 67
Zocchi, A., Gieles, M., Hénault-Brunet, V., & Varri, A. L. 2016, MNRAS, 462, 696